buildings

MDPI

Article

Bond Behavior of Carbon Fabric-Reinforced Matrix Composites: Geopolymeric Matrix versus Cementitious Mortar

Feras Abu Obaida, Tamer El-Maaddawy * and Hilal El-Hassan

Department of Civil and Environmental Engineering, United Arab Emirates University, Al Ain P.O. Box 15551, United Arab Emirates; 201770001@uaeu.ac.ae (F.A.O.); helhassan@uaeu.ac.ae (H.E.-H.)
* Correspondence: tamer.maaddawy@uaeu.ac.ae

Abstract: This study aims to examine the potential use of a geopolymeric matrix as a sustainable alternative to commercial mortars in carbon fabric-reinforced matrix composites. Single-lap shear tests were conducted to examine the bond behavior at the fabric-matrix interface. Test parameters included the type of matrix (geopolymeric and cementitious matrices) and the bonded length (50 to 300 mm). The geopolymeric matrix was a blend of fly ash/ground granulated blast furnace slag activated by an alkaline solution of sodium silicate and sodium hydroxide. The bond behavior of the geopolymeric-matrix specimens was characterized and compared to that of similar specimens with a cementitious matrix. The specimens failed due to fabric slippage/debonding at the fabric-matrix interface or fabric rupture. The effective bond lengths of the geopolymeric- and cementitious-matrix specimens were 150 and 170 mm, respectively. The geopolymeric-matrix specimens exhibited higher fabric strains, higher ultimate loads, and a steeper strain profile along the bonded length than those of their cementitious-matrix counterparts. New bond-slip models that characterize the bond behavior at the fabric-matrix interface for geopolymeric- and cementitious-matrix specimens were developed. Both models exhibited equal maximum shear stress of 1.2 MPa. The geopolymeric-matrix model had, however, higher fracture energy and higher slip at maximum shear stress than those of the cementitious matrix model.

Keywords: carbon fabric; matrix; bond; slip; geopolymer; cementitious

Citation: Abu Obaida, F.; El-Maaddawy, T.; El-Hassan, H. Bond Behavior of Carbon Fabric-Reinforced Matrix Composites: Geopolymeric Matrix versus Cementitious Mortar. *Buildings* **2021**, *11*, 207. https://doi.org/10.3390/buildings11050207

Academic Editor: Francesco Colangelo

Received: 10 April 2021
Accepted: 11 May 2021
Published: 15 May 2021

1. Introduction

Fabric-reinforced cementitious matrix (FRCM) composite-based systems have been widely used in flexural strengthening, shear strengthening, column confinement, seismic retrofitting of beam-column connections, and masonry-infilled reinforced concrete frames [1–3]. In addition to their non-corrosive nature, FRCM systems involve the use of cement-based mortars as a matrix rather than epoxy. This results in an enhancement in the bond at the matrix-substrate interface and improvement in the fire resistance of the composite system relative to those of epoxy-based composite systems [1–3]. State-of-the-art reviews on the strengthening of masonry and reinforced concrete (RC) structures with FRCM systems have been published recently by Awani et al. [2] and Koutas et al. [3].

Fabrics used in FRCM systems are typically coated to improve the adhesion and the bond at the fabric-matrix interface and to facilitate handling and installation. Changing the properties of the fabric surface by sizing or coating can enhance the chemical bond and friction at the fabric-matrix interface and mitigate telescopic failure, thereby allowing full utilization of fabric tensile properties and improving the performance of FRCM composite systems [4–8].

The coating type and thickness affect the performance of the FRCM composites [4,5]. Polymer-based coating increased the tensile and shear-bond capacities of FRCM systems [4]. The use of coating made of flexible epoxy and sand improved the adhesion between the mortar and the fabric and changed the mode of failure from fabric slippage to fibers

rupture [4]. The thickness of the polymer coating had a significant effect on data scattering, mode failure, and hence the performance of FRCM composites [5]. Fabric rupture mode of failure was consistently observed in thin-coated specimens, whereas thick-coated specimens exhibited mixed/scattered results [5].

Furthermore, silica coating resulted in a significant improvement in the interphase bond in fabric-reinforced mortar composites [6]. The use of silica coating was, however, less effective than a polymer coating in improving the interphase bond and mechanical properties of fabric-reinforced mortar composites [6]. Coating of fabrics with styrene-butadiene rubber (SBR) offers an improvement in the abrasion resistance and the adhesion at the fiber-matrix interface [7,8]. A microstructural investigation revealed a variation in the thickness of the SBR-coating along the fiber length [7]. The presence of such defects at the fabric-coating interfaces of industrially produced fabrics affected the failure mode even within small regions in the FRCM composites. SBR-coating peeling-off together with the cementitious matrix took place at the location of defects (i.e., zones having thin SBR-coating). In such regions, failure of adherence between the carbon fiber and the SBR-coating took place. In regions with no defects, the SBR-coating remained adhered to the fibers with some matrix residue on them. Such regions failed due to the stripping of the matrix [7].

The bond behavior at the fabric-matrix interface in FRCM systems is a critical aspect that affects the design and overall performance of strengthened RC structures. Therefore, research related to studying the bond behavior of FRCM systems and the development of interfacial bond-slip models at the fabric-matrix interface has attracted many researchers in the field. Several investigations compared the bond behavior of FRCM composites with different types of fabric grids and matrices. Hashemi and Al-Mahaidi [9] examined the bond behavior of fabric textiles and fabric sheets. The test results showed a 30% higher bond capacity in the former, owing to penetration of the mortar through the fabric grid and improved mechanical interlock. In other work, the bond behavior of FRCM composites comprising glass and carbon fabrics was studied using single-lap direct-shear tests [10]. Specimens with a glass fabric exhibited higher peak loads than those of their counterparts with carbon fabric, indicating a better bond for the glass FRCM composites. The properties of the matrix had no noticeable effect on the response of the tested specimens. Awani et al. [11] reported that fabric-reinforced epoxy (FRE) specimens showed higher loads in double shear bond tests relative to those of their FRCM counterparts. The former failed abruptly due to fabric rupture, while the latter experienced debonding at the fabric-matrix interface along with excessive slippage of the fabric. Barducci et al. [12] examined the bond behavior of FRCM composites made of basalt textile coupled with lime-based or commercial mortars applied on clay bricks using single and double-lap shear tests. Experimental findings showed that the commercial mortars provided better bond strength than that of their lime-based counterparts.

The majority of published works reported that the bond capacity increased with the bonded length up to an effective length, after which the bond strength remained constant. In fact, effective bond lengths in the range of 150–300 mm were reported [10,13–18]. Conversely, the bonded width had little or no effect on the bond strength [15,16,19,20]. Failure of FRCM composites was typically in the form of a single or combination of different modes, including interfacial debonding between the fabric and cementitious matrix, slippage of the fabric, and tensile failure of the longitudinal fiber bundles [18,21].

The production of cement results in a substantial carbon dioxide emission. It also consumes a significant amount of non-renewable natural resources. To overcome these problems, few researchers investigated the potential use of cement-free geopolymeric matrices rather than cementitious mortars to produce sustainable fabric-reinforced geopolymeric matrix (FRGM) strengthening solutions. Vasconcelos et al. [22] employed a metakaolin-based geopolymer matrix as a sustainable alternative to commercial mortars. The findings showed that the proposed inorganic matrix was effective in increasing the strength of RC beams. A study by Menna et al. [23] on strengthened concrete beams highlighted a very good adhesion between a metakaolin-based geopolymer matrix, concrete substrate,

and steel cords. In contrast, when carbon fabrics were used, failure of the beams was in the form of debonding at the fabric-matrix interface. The fluidity of the matrix affected the bond performance. Bencardino et al. [24] examined the bond behavior of a stainless steel strip embedded in a geopolymeric matrix. The specimens experienced debonding at the steel cords-matrix interface. An effective bond length of 200 mm was required to develop the maximum bond strength. A bond-slip model characterizing the bond behavior at the steel cords-matrix interface was developed. Although the study by Bencardino et al. [24] focused on the bond behavior through single-lap shear tests, the reinforcement was in the form of stainless steel chords rather than non-metallic fabrics.

2. Research Significance

Despite the widespread use of cement-based mortars in FRCM systems and their advantages such as fire resistance and compatibility with the concrete substrate, manufacturing and producing cementitious mortars have environmental and ecological drawbacks. There are limited studies available in the literature that involved the use of geopolymeric matrices as an alternative sustainable solution to commercial cementitious mortars. Available studies on nonmetallic composite-based systems utilizing geopolymeric matrices focused mainly on investigating the carrying capacity of strengthened RC beams without characterizing the bond behavior at the fabric-matrix interface. As such, there is a lack of knowledge on the bond behavior of nonmetallic composite strengthening systems utilizing carbon fabrics and a geopolymeric matrix. Characterization of the bond behavior at the fabric-geopolymeric matrix interface is needed before geopolymers can be routinely used as matrices in structural strengthening applications. This paper aims to fill this gap through single-lap shear testing and analytical modeling. Outcomes of the study offer a valuable contribution to the state of the art by presenting new experimental results, developing new bond-slip models, and offering new knowledge on the bond behavior of carbon fabric-reinforced geopolymeric matrix concrete joints.

3. Experimental Program

Single-lap shear tests were carried out on 18 specimens to investigate the bond behavior of carbon fabric-reinforced matrix composites bonded to concrete. The varied parameters were the type of matrix (cementitious and geopolymeric) and the bonded length (l_b) which ranged from 50 to 300 mm.

3.1. Materials

3.1.1. Concrete

The concrete mix used in the current study included American Society for Testing and Materials (ASTM) Type I ordinary Portland cement as a binding material (Al Ain Cement, Al Ain, UAE). The concrete mix proportions by weight were cement: fine aggregates: coarse aggregates: w/c of 1:2.2:2.9:0.45. The fine aggregates comprised a 1:1 combination of dune sand and 5 mm crushed black sand. A blend of 10 and 20 mm (nominal maximum size) dolomitic limestone served as coarse aggregate. The properties of the coarse and fine aggregates are presented elsewhere [25]. Concrete samples used for evaluating the mechanical properties were in the form of 150 mm cubes and 150 mm × 300 mm (diameter × height) cylinders. For each mechanical property, three replicate samples were prepared and tested according to the BS and ASTM procedures [26–29]. The average cube compressive strength, cylinder compressive strength, and splitting tensile strength of the concrete were 48, 40, and 3.30 MPa, respectively.

3.1.2. Geopolymeric Matrix

The geopolymeric matrix was formulated using a precursor binder, fine aggregates, and an alkaline activator solution. Class F fly ash and slag were employed as binding materials [30]. Their relative density was determined as 2.32 and 2.70, respectively, while their respective Blaine fineness was 3680 and 4250 cm^2/g. The fly ash was obtained from Ashtech

International, Dubai, UAE. Fine aggregates were in the form of desert dune sand, with a particle size ranging between 50 and 600 microns, a relative density of 2.57, and a unit weight of 1670 kg/m^3. The chemical composition, particle size distribution, morphology, and mineralogy of as-received materials are published elsewhere [31–33]. The alkaline activator solution was a combination of sodium silicate (SS) and sodium hydroxide (SH). The sodium silicate was a commercial-grade N solution with a mass chemical composition of 26.3, 10.3, and 63.4% of SiO_2, Na_2O, and H_2O, respectively. The sodium hydroxide was formulated into a 14 M molarity by combining 98%-pure SH flakes with tap water. A polycarboxylic ether polymer-based superplasticizer was used to enhance the workability without compromising the mechanical properties. The geopolymeric matrix mix was designed with equal proportions of fly ash and slag. Combining fly ash and slag aimed to eliminate the need for heat curing typically required in fly ash-based geopolymers, while also reducing the drying shrinkage observed in slag-based equivalents. The content of the binder was 625 kg/m^3, dune sand was 937.5 kg/m^3, sodium silicate was 187.5 kg/m^3, sodium hydroxide was 125 kg/m^3, and superplasticizer was 12.5 kg/m^3. Such mixture proportions values were selected based on past research [34]. Geopolymer matrix samples used for evaluating the mechanical properties were 50 mm cubes and 100 mm × 200 mm (diameter × height) cylinders. Tests were conducted on triplicate samples according to the ASTM standards [35,36]. The average cube compressive strength, cylinder compressive strength, and splitting tensile strength of the geopolymeric matrix were on average 43, 34, and 3.0 MPa, respectively. The Young's modulus was, on average, 7 GPa.

3.1.3. Cementitious Matrix

The cementitious matrix employed herein was a cement-based commercial adhesive manufactured by S&P Clever Reinforcement Company AG, Seewen, Switzerland. Cementitious matrix samples used for evaluating the mechanical properties were 50 mm cubes and 100 mm × 200 mm (diameter × height) cylinders. Tests were conducted on triplicate samples according to the ASTM standards [35,36]. The average cube compressive strength, cylinder compressive strength, and splitting tensile strength of the cementitious matrix were on average 42, 36, and 2.4 MPa, respectively. The Young's modulus was, on average, 28 GPa.

3.1.4. Carbon Fabric

A commercial amorphous silica-coated carbon fabric was used in the present study. In addition to the facilitation of handling and installation, silica coating offers an improvement in the bond at the fabric-matrix interface [6]. The fabric comprised unidirectional carbon fiber bundles with a center-to-center spacing of 17 mm (Figure 1). The properties of the carbon fabric, as provided by the manufacturer [37], are listed in Table 1. The width, b_{f0}, and thickness, t_{f0}, of one fiber bundle measured by the authors were approximately 5.0 and 0.54 mm, respectively. This corresponds to a cross-sectional area per unit length of 159 mm^2/m, which is consistent with that provided by the manufacturer (157 mm^2/m).

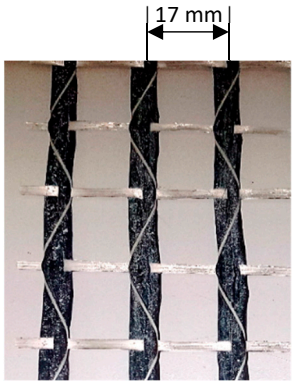

Figure 1. Carbon fabric.

Table 1. Fabric properties (Data from [37]).

Property	Unit	Value
Weight per unit area	g/m^2	281
Tensile strength, f_{fr}	MPa	4300
Modulus of elasticity, E_f	GPa	240
Elongation at break, ε_{fr}	%	1.80
Cross-sectional area per unit length [1]	mm^2/m	157

[1] One fiber bundle has an actual measured width of b_{f0} = 5.0 mm and thickness of t_{f0} = 0.54 mm, which corresponds to an actual cross-sectional area of 159 mm^2/m.

3.2. Specimens Preparation

Specimens of the single-lap shear test comprised one composite layer of FRCM or FRGM bonded to a 550-mm-long concrete prism having a cross-section of 150 mm × 150 mm. Concrete specimens' preparation was carried out in accordance with ASTM C192 [26]. The concrete mixture was prepared by mixing the solid constituents, including the cement, fine aggregates, and coarse aggregates, in a laboratory mechanical mixer for 3 min. Subsequently, the water was gradually added into the mixed dry ingredients and further mixed for another 2 min to ensure uniformity and homogeneity of the mix. Fresh concrete was then poured into molds and compacted using a vibrating table for 10 s. They were covered with a plastic sheet for 24 h, demolded, and placed in a water tank until testing.

Geopolymer and cementitious matrices preparation was carried out under a room temperature of 23 ± 2 °C and relative humidity of 50 ± 5%. For the geopolymer matrix, the dry components, comprising fly ash, slag, and dune sand, were mixed for 3 min in a pan mixer. In a separate mixer, the sodium hydroxide was mixed with the specific quantity of water and allowed to rest to dissipate the heat from the exothermic reaction. The sodium hydroxide solution was then mixed with the sodium silicate solution and set aside until it reached room temperature. The superplasticizer was added to the formulated alkaline activator solution and subsequently mixed into the dry ingredients for 3 min. For the cementitious matrix, the cement-based commercial binder was gradually added to the water at a water-to-binder ratio of 0.152, as recommended by the manufacturer. The mixture was mixed for 3 min until it became homogeneous and lump-free and then left to rest for 1–2 min before application.

The composite layer, with a geopolymer or cementitious matrix, was bonded to the 150 mm × 550 mm concrete face. The width of the matrix in all specimens was kept constant at 50 mm. The length and width of the designated bonded area were marked on the concrete surface. The marked concrete surface was then roughened using a waterjet. The wet concrete surface was then left to dry to achieve a saturated surface dry (SSD) condition prior to the application of the composite layer. Fresh mortar was then placed on this rough SSD concrete surface to a thickness of approximately 4 mm. The carbon fabrics were pre-cut into 50 mm-wide strips and different bonded lengths ranging from

50 to 300 mm. The pre-cut fabric was placed on top of the first mortar layer then pushed into it to ensure proper impregnation. A second mortar layer was then placed on top of the fabric, resulting in a total composite thickness of approximately 10 mm. The strengthening composite layer was cured for 7 days using damp burlap under a room temperature of 23 ± 2 °C and relative humidity of 50 ± 5%. No thermal curing techniques were adopted in the present study.

3.3. Test Setup

A schematic of the test setup is shown in Figure 2a, whereas a test in progress is shown in Figure 2b. The concrete prism was restrained against movement during testing by means of a rigid closed steel frame bolted to the base of a universal MTS testing machine manufactured by MTS Systems Corporation, Eden Prairie, USA. The fabric was pulled out of the matrix bonded to the restrained concrete prism in a push-pull configuration. Two aluminum plates were bonded to the end of the bare fabric at the location of the tensile grip to ensure a uniform distribution of the load across the fibers during testing. Tests were conducted under displacement control at a rate of 0.5 mm/min using the universal MTS testing machine. The global slip was measured using two linear variable displacement transducers (LVDTs) reacted off of a thin aluminum L-shaped plate attached to the bare fabric in the proximity of the bonded area (i.e., just outside the composite bonded area). The fabric in two of the specimens having a bonded length of 300 mm was instrumented with six strain gauges (SG) along the bonded length at 50 mm spacing. The loads, strains, and displacements were recorded by means of a data acquisition system.

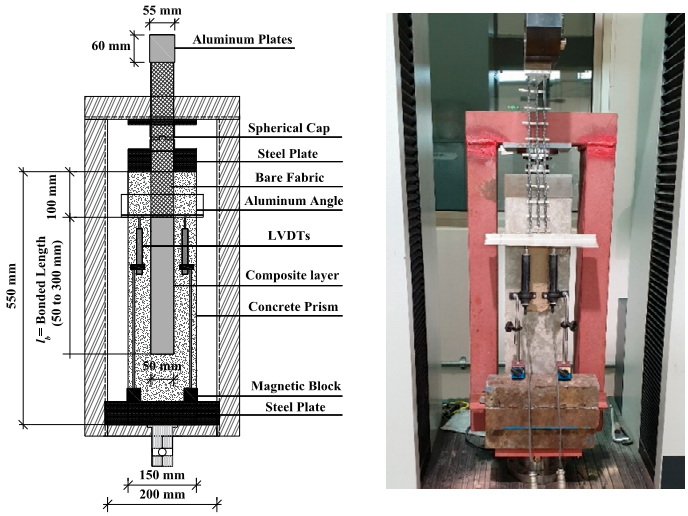

Figure 2. Bond test: (**a**) A schematic of the test specimen and set-up; (**b**) A test in progress.

4. Experimental Results

4.1. Maximum Load and Effective Bond Length

The maximum loads exhibited by the tested specimens are summarized in Table 2. The maximum loads of the geopolymeric-matrix specimens, except GM-250, were on average 71% higher than those of their cementitious-matrix counterparts. The higher loads exhibited by the geopolymeric-matrix specimens implies better bond at the fabric-matrix interface. The average peak load of GM-250 with a geopolymeric matrix was approximately 84% of that of CM-250 with a cementitious matrix. One of the duplicate specimens of GM-250 (S1) had pre-existing transverse shrinkage cracks along the bonded length of the composite, which may have reduced its load-carrying capacity. The fabric of the other duplicate specimen of GM-250 (S2) exhibited a slight in-plan rotation at the end of the test which overstressed some of the fabric bundles thus promoting a premature fabric rupture mode of failure. Specimen CM-300 exhibited also an in-plan rotation during testing,

which overstressed some of the fabric bundles and reduced the specimen's load capacity to a level lower than those of specimens CM-200 and CM-250. The presence of pre-existing shrinkage cracks in the matrix and the possibility of rotation of fabrics during tensile testing are reported in the literature by other researchers in similar bond tests [15,16,18,20].

Table 2. Test results.

Group	Specimen	Bonded Length (mm)	Maximum Load (kN)		Average Peak Load (kN)	Mode of Failure [2]
			S1 [1]	S2 [1]		
Cementitious matrix specimens	CM-50	50	2.11	N.A.	2.11	S1: Mode I, S2: N.A.
	CM-100	100	1.45	2.08	1.76	S1: Mode II, S2: Mode I
	CM-150	150	5.59	3.42	4.51	S1: Mode I, S2: Mode II
	CM-200	200	4.67	5.07	4.87	S1: Mode II, S2: Mode II
	CM-250	250	6.88	N.A.	6.88	S1: Mode III, S2: N.A.
	CM-300	300	4.32	N.A.	4.32	S1: Mode III, S2: N.A.
Geopolymeric matrix specimens	GM-50	50	3.78	2.16	2.97	S1: Mode I, S2: Mode II
	GM-100	100	4.89	4.12	4.51	S1: Mode I, S2: Mode II
	GM-150	150	5.70	N.A.	5.70	S1: Mode I, S2: N.A.
	GM-200	200	N.A.	7.34	7.34	S1: N.A., S2: Mode III
	GM-250	250	6.22	5.29	5.76	S1: Mode II, S2: Mode III
	GM-300	300	N.A.	7.89	7.89	S1: N.A., S2: Mode III

[1] Specimen number. [2] Mode I: slippage of fabric without cracking; Mode II: matrix cracking followed by slippage of fabric/interfacial debonding; Mode III: rupture of fabric outside the matrix.

Maximum load values of specimens of the present study are in the same range as those published in the literature by other researchers for PBO FRCM [15,16] and stainless steel-reinforced geopolymeric matrix composites [24]. The maximum load of similar PBO FRCM bond specimens reported in the literature, with a bonded width of 34 to 60 mm and bonded length of 100 to 330 mm, was in the range of 0.97 to 8.29 MPa [15,16]. Similarly, stainless steel-reinforced geopolymeric matrix bond specimens, having a bonded width of 50 mm and a bonded length of 100 to 400 mm, exhibited a maximum load in the range of 4.8 to 7.9 kN [24].

The effective bond length (l_{eff}) is defined as the minimum length required to fully establish the bond mechanism/stress transfer zone (STZ) [15,16,38]. For FRP joints, the debonding load coincides with the maximum load which remains almost unaltered when l_b exceeds l_{eff} [15,16,18,39]. For FRCM joints with $l_b > l_{eff}$, the maximum load is slightly greater than the debonding load because of the presence of friction/interlocking between the fabric and matrix after the onset of debonding [15,16,18,38]. As a result, FRCM joints with $l_b > l_{eff}$ exhibit a non-proportional increase in the maximum load with an increase in the bonded length at a rate lower than that exhibited by similar specimens with $l_b \leq l_{eff}$.

The maximum loads exhibited by the cementitious and geopolymeric specimens are plotted against the bonded length in Figure 3a,b, respectively. The maximum load increased almost linearly with an increase in the bonded length up to an effective bond length, l_{eff}, after which the maximum load continued to increase but at a reduced rate. A regression analysis was first conducted to plot the best-fit polynomial relationship of experimental data. The point where a major change in the slope of the best-fit polynomial relationship was then identified by inspection. An idealized bilinear relationship was then developed. The first part of the idealized bilinear relationship was obtained by connecting the origin of the curve to the point identified earlier on the best-fit polynomial curve where a major change in slope took place. In turn, the second part of the idealized bilinear relationship was attained by connecting the point identified earlier on the best-fit polynomial curve causing a major change in slope to the last point of the best-fit polynomial curve. Based on the idealized bilinear relationship shown in the figures, the effective bond length was approximately 170 mm for the cementitious-matrix specimens and 150 mm for the geopolymeric-matrix specimens. Although experimental data used in Figure 3 are

relatively scattered, particularly for the cementitious-matrix specimens, effective bond length values obtained from this figure are consistent with those reported in the literature for FRCM joints (150 to 300 mm) [15–17,38]. Also, Bencardino et al. [24] reported an effective bond length of 200 mm for a stainless steel reinforced-geopolymeric matrix composite system.

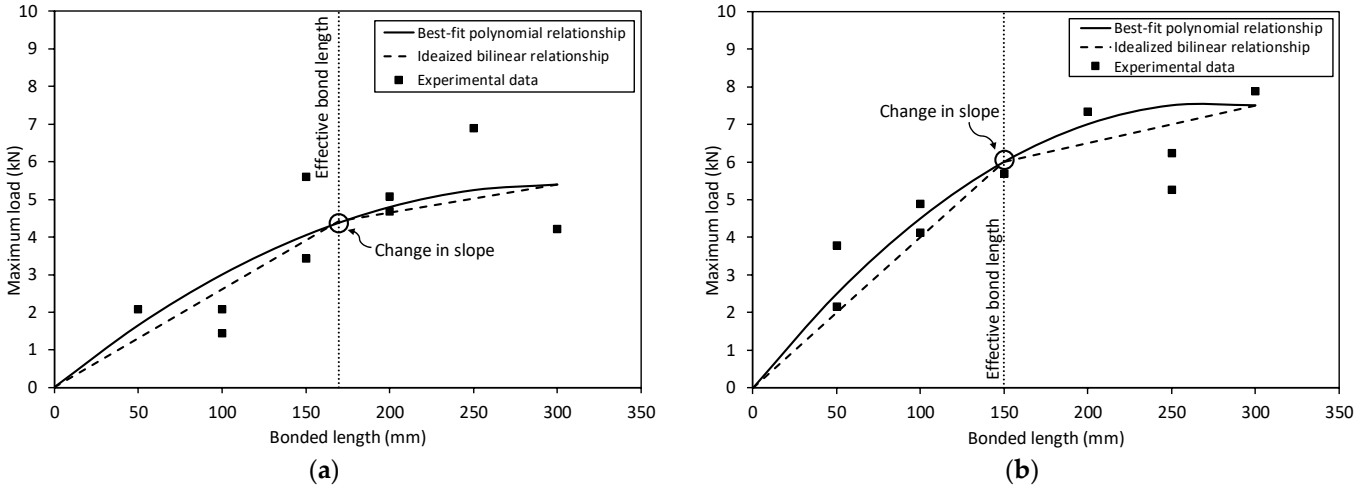

Figure 3. Maximum load-bond length relationship: (**a**) Cementitious-matrix specimens; (**b**) Geopolymeric-matrix specimens.

4.2. Failure Mode

Three distinct modes of failure were observed in the present study (Figure 4); Mode I: slippage of the fabric without cracking of the matrix, Mode II: transverse/longitudinal cracks followed by slippage of the fabric and debonding at the fabric-matrix interface, and Mode III: rupture of the fabric outside the matrix. This is consistent with typical failure modes reported in the literature for FRCM systems [18,21].

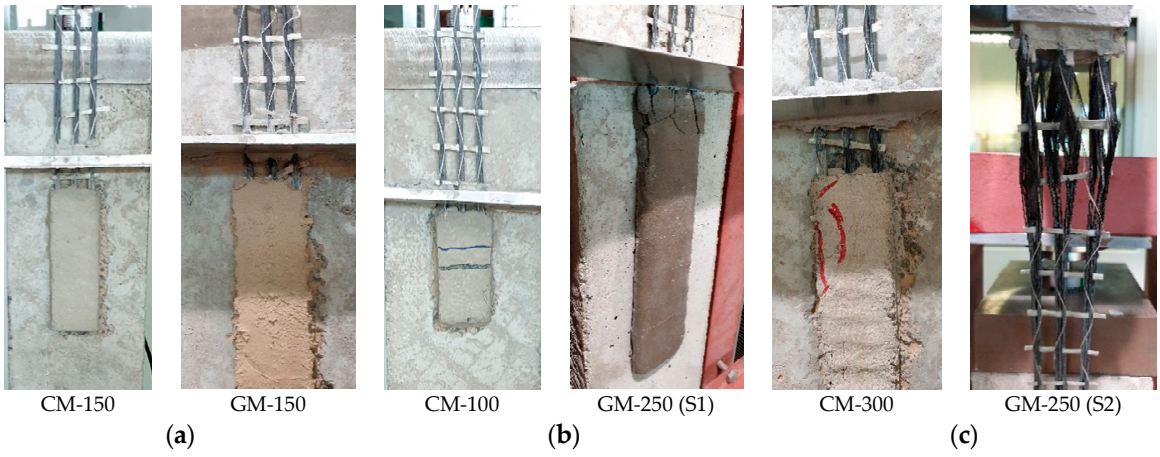

Figure 4. Typical modes of failure: (**a**) Mode I; (**b**) Mode II; (**c**) Mode III.

Mode II comprised the formation of one or two transverse cracks. Some specimens exhibited also longitudinal cracks along with one or more of the fabric bundles prior to failure. Specimens with Mode III did not exhibit cracks prior to rupture except specimen CM-250, which had one transverse crack close to the loaded end and two longitudinal cracks along with the exterior fiber bundles. Typical crack patterns observed in the current study are shown in Figure 5. Specimens with $l_b \leq 100$ mm exhibited one transverse crack in the middle of the bonded length which weakened the composite action at the fabric-matrix interface. As the load progressed, the crack widened, slippage of fabric occurred, followed

by debonding at the fabric-matrix interface. Specimen CM-100 exhibited one additional transverse crack at a distance of 20 mm away from the middle crack toward the loaded end. Specimens with l_b of 150 and 200 mm exhibited two transverse cracks in addition to one longitudinal crack along with the middle fiber bundle near the loaded end. The distance between the transverse cracks was 75 mm for the cementitious-matrix specimens, whereas it was 50 mm for the geopolymeric-matrix specimens. Smaller spacing between transverse cracks may indicate better bond at the fabric-matrix interface. Specimens with l_b = 250 mm exhibited one transverse crack at a distance 50 mm away from the loaded end in addition to longitudinal cracks along with the fiber bundles.

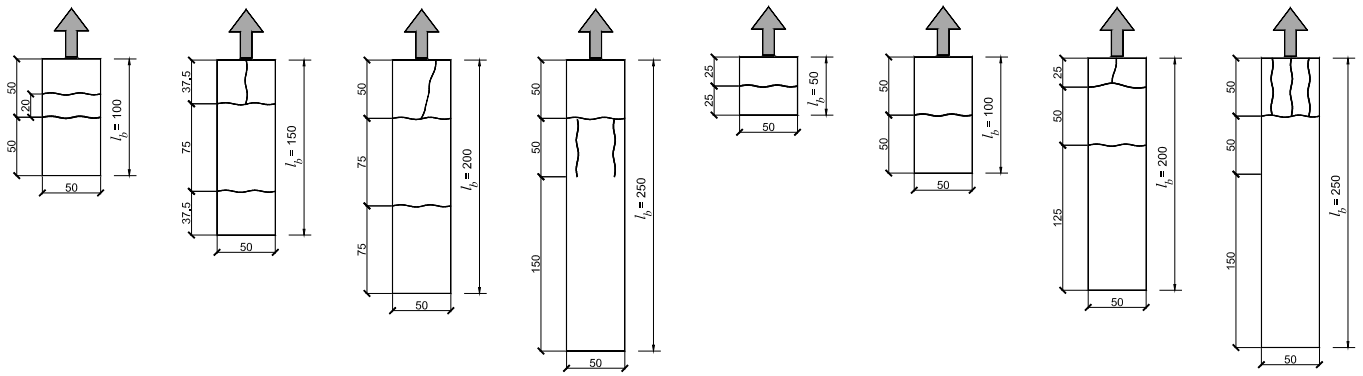

(**a**) (**b**)

Figure 5. Crack patterns at failure: (**a**) Cementitious-matrix specimens; (**b**) Geopolymeric-matrix specimens.

Mode III, which involved rupture of the fabric outside the matrix, occurred only in some of the specimens with $l_b > l_{eff}$. In the absence of a debonding mode of failure, the fabric may experience slight in-plan rotation at the end of the test which would result in overstressing some fabric bundles, thus promoting a premature fabric rupture mode of failure. This is consistent with other findings in the literature which reported possible rotation of fabrics in similar bond tests [15,16,18,20,24].

The failure modes exhibited by the tested specimens are given in Table 2. All cementitious-matrix specimens exhibited either Mode I or Mode II except specimen CM-250, which showed Mode III that involved rupture of the fabric. Three geopolymeric-matrix specimens, with a bonded length in the range of 200 to 300 mm exhibited rupture of fabric mode of failure (Mode III). Other geopolymeric-matrix specimens exhibited either Mode I or Mode II.

4.3. Load-Global Slip Response

The global slip is defined as the relative displacement between points on the bare fabric strip just outside the composite bonded area and the adjacent surface of the concrete prism. The load-global strip responses of representative specimens with cementitious and geopolymeric matrices are plotted in Figure 6a,b, respectively. The response was dependent on the bonded length and the failure mode as idealized in Figure 7.

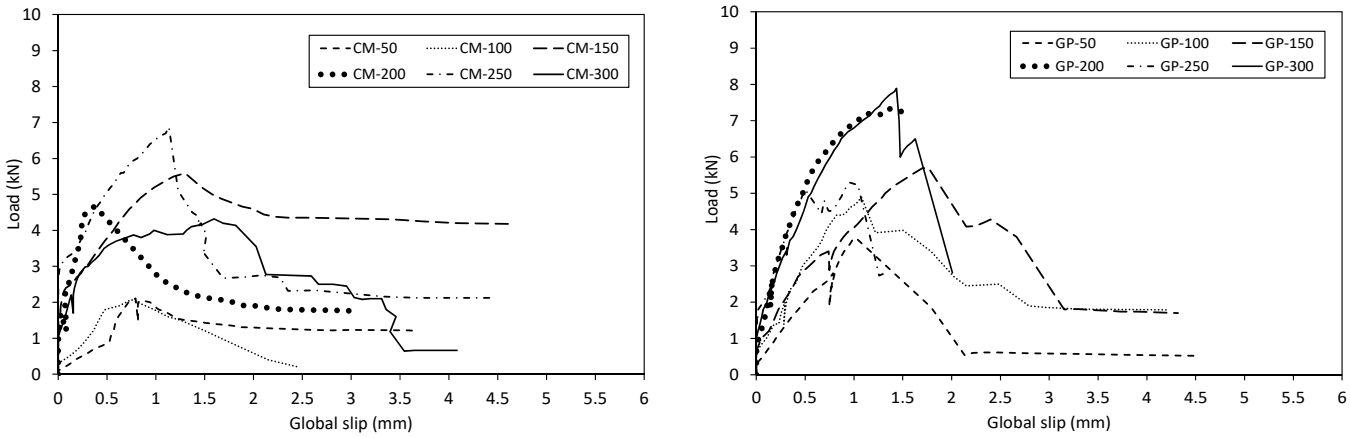

(**a**) (**b**)

Figure 6. Load-global slip curves: (**a**) Cementitious-matrix specimens; (**b**) Geopolymeric-matrix specimens.

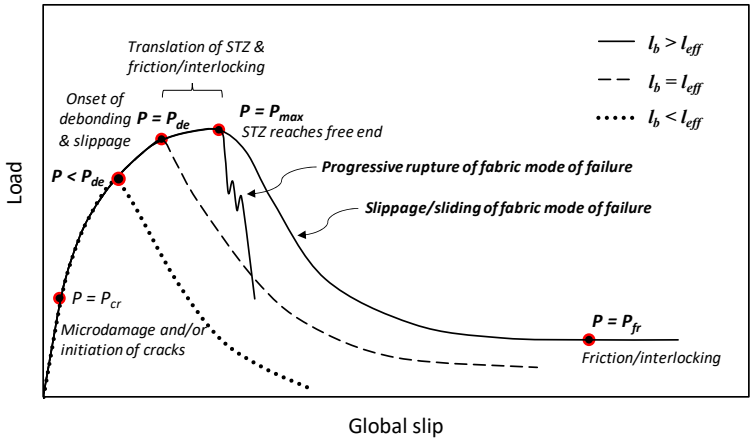

Figure 7. Idealized load-global slip response.

Initially, all specimens exhibited a linear response until the initiation of cracks or occurrence of microdamage at the fabric-matrix interface at a load value of P_{cr}. Following cracking and/or the interfacial microdamage, the load continued to increase in a nonlinear fashion. Specimens with $l_b = l_{eff}$ failed when the load reached the debonding load (P_{de}) at which the STZ was fully established (STZ is the zone in which stresses are transferred from the fabric to the matrix). Specimens with $l_b < l_{eff}$ failed at load values less than P_{de}. For specimens with $l_b > l_{eff}$, the load continued to increase after the onset of debonding but at a reduced rate until the STZ reached the free end and/or rupture of the fabric occurred. This phenomenon occurred due to the presence of friction and interlocking between the fabric and matrix. The post-peak behavior was depended on the mode of failure. Specimens with Mode I and II, which involved slippage of the fabric without rupture, exhibited a progressive load drop to a residual strength. In the final stage, the load remained almost constant at P_{fr} caused by the presence of friction/matrix-fabric interlocking. In contrast, specimens with Mode III, which involved rupture of the fabric, exhibited a sudden drop in load at peak and, in some cases, followed by a series of drops due to progressive rupture of the fiber bundles.

4.4. Measured Fabric Strains

The fabric strain profile along the bonded length at different load increments of specimens CM-300 and GM-300 are depicted in Figure 8a,b respectively. For specimen CM-300, only SG5 and SG6 nearest to the loaded end were strained at a load value of 0.25 Pmax. Strain gauge SG4 located at a distance 175 mm from the free end started to

strain at 0.5 Pmax whereas SG3 located at a distance 125 mm from the free end remained unstrained up to a load value of 0.75 Pmax. Strain gauges SG1 and SG2 nearest to the free end remained unstained till the end of the test.

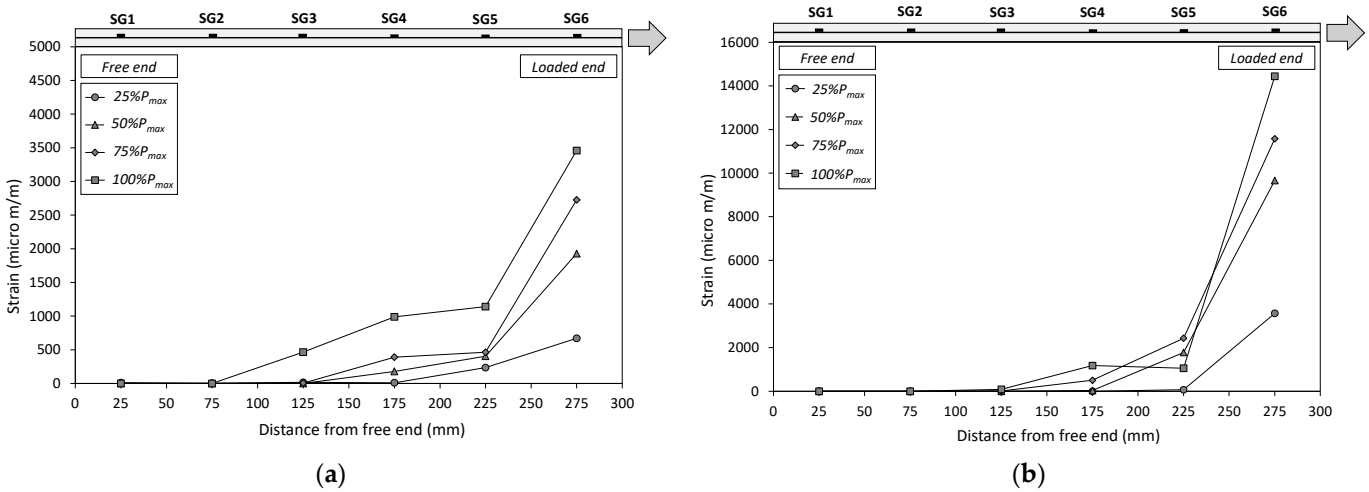

Figure 8. Longitudinal fabric strain profile along the bonded length: (**a**) specimen CM-300; (**b**) specimen GM-300.

Figure 8b shows the fabric strain profile of specimen GM-300. The fabric strains at the proximity of the loaded end measured by SG6 were significantly higher than those of other strain gages, indicating a shear stress concentration near the loaded end. Strain gauge SG4 located at a distance 175 mm from the free end remained unstrained up to 0.5 Pmax whereas SG1, SG2, and SG3, located at respective distances 25, 75, and 125 mm from the free end remained unstrained until the end of the test.

Specimen GM-300 exhibited higher fabric strains near the loaded end and a steeper strain profile than those of specimen CM-300 which signified better bond at the fabric-matrix interface. The better bond properties at the interface resulted in higher peak loads.

5. Development of Bond-Slip Models

The relationship between the fabric strain at the loaded end, ε_f, and the corresponding slip, s, can be expressed by Equation (1), noting that ε_f, is calculated using Equation (2), where A, B = parameters from regression analysis, b_{f0} = width of one fiber bundle, E_f = Young's modulus of the fabric, n = number of fiber bundles in the fabric, and t_{f0} = thickness of one fiber bundle.

$$\varepsilon_f = A \times (1 - e^{-Bs}) \quad (1)$$

$$\varepsilon_f = P/(n \times b_{f0} \times t_{f0} \times E_f) \quad (2)$$

The maximum load, P_{max}, can then be calculated using Equation (3), where f_{fr} = fabric tensile strength [24,39].

$$P_{max} = A \times E_f \times n \times b_{f0} \times t_{f0} \leq n \times b_{f0} \times t_{f0} \times f_{fr} \quad (3)$$

The following procedure was adopted to determine the parameters A and B of the specimens with $l_b > l_{eff}$, and compute the corresponding analytical maximum loads.

- For a given value of the load, P, the corresponding strain in the fabric, ε_f, at the loaded end was calculated using Equation (2).
- A relationship between the fabric strain calculated at the loaded end, ε_f, and the corresponding slip, s, measured experimentally was plotted.
- A nonlinear regression analysis was performed to derive the parameters A and B that best fit Equation (1).
- The analytical maximum load was calculated using Equation (3).

The relationship between the fabric strain at the loaded end, ε_f, and the corresponding slip, s, can be expressed by Equation (1), noting that ε_f, is calculated using Equation (2), where A, B = parameters from regression analysis, b_{f0} = width of one fiber bundle, E_f = Young's modulus of the fabric, n = number of fiber bundles in the fabric, and t_{f0} = thickness of one fiber bundle.

$$\tau = A^2 \times B \times E_f \times t_{f0} \times (e^{-Bs} - e^{-2Bs}) \quad (4)$$

Once parameters A and B are determined and the τ-s relationship is established, other key parameters can be computed. The slip at maximum shear stress (s_m), given by Equation (5), is obtained by computing the value of the slip at which $d\tau/ds = 0$ (i.e., $s = s_m$ when $d\tau/ds = 0$). The maximum shear stress at the fabric-matrix interface (τ_m), given by Equation (6), is obtained by substituting Equation (5) into Equation (4). The fracture energy is then calculated using Equation (7).

$$s_m = 0.693/B \quad (5)$$

$$\tau_m = 0.25 \times A^2 \times B \times E_f \times t_{f0} \quad (6)$$

$$G_f = 0.5 \times A^2 \times E_f \times t_{f0} \quad (7)$$

It should be noted that Zou et al. [38] proposed to add a constant term, τ_f, to the right side of Equation (4) in an effort to include the friction stress at the end of the descending branch of the shear stress-slip relationship. The constant friction stress located at the end of the descending branch of the relationship proposed by Zou et al. [38] was in the range of 0.08 to 0.12 MPa which corresponded to approximately 5 to 9% of the respective maximum shear stress, and hence was ignored in Equation (4) adopted in the current study. Bond-slip models at the fabric-matrix interface are necessary for finite element modeling/numerical simulation of large-scale reinforced concrete elements strengthened with FRCM/FRGM systems. The exclusion of such a small value of friction stress at the end of the descending branch of the bond-slip model would have no effect on the structural behavior of large-scale RC elements strengthened with FRCM/FRGM composite systems.

The shear stress-slip relationships developed in the current study for the cementitious- and geopolymer-matrix specimens with $l_b > l_{eff}$ are shown in Figure 9a,b, respectively, whereas the key parameters and a comparison between analytical and measured maximum loads are given in Table 3. It can be seen that the analytical maximum loads are in good agreement with those measured experimentally. The analytical maximum loads were within 11% error band, which can be considered within the acceptable margin of error.

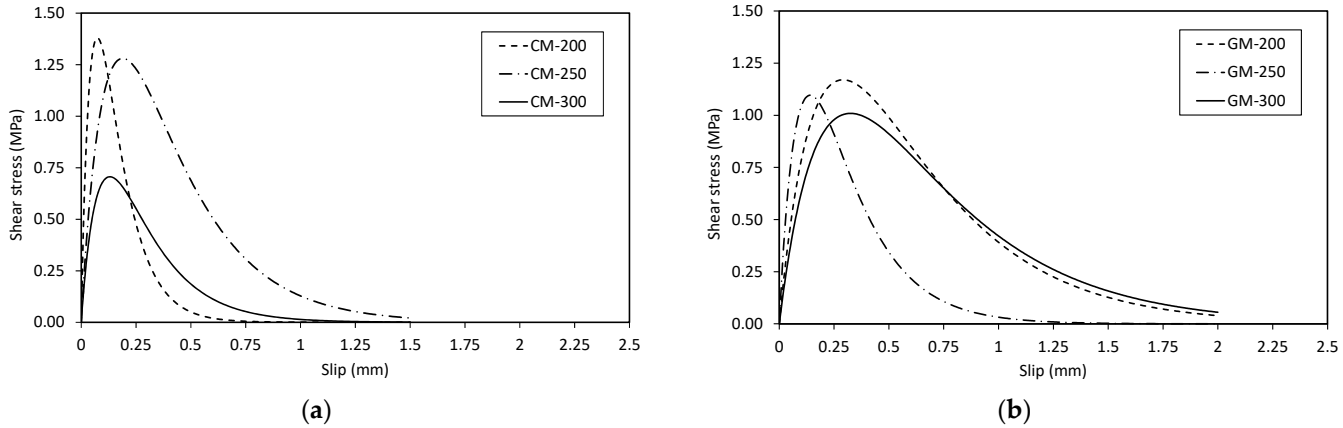

Figure 9. Shear stress-slip relationships for the tested specimens with $l_b > l_{eff}$: (**a**) Cementitious-matrix specimens, (**b**) Geopolymeric-matrix specimens.

Table 3. Analytical results and comparison with measured maximum loads.

Group	Specimen	A ($\times 10^{-3}$)	B (mm^{-1})	G_f (N/mm)	τ_m (MPa)	s_m (mm)	Maximum Load (kN) Analytical	Maximum Load (kN) Experimental	Error [1] (%)
Cementitious matrix specimens	CM-200	2.10	9.38	0.29	1.38	0.07	4.14	4.67	−11
	CM-250	3.28	3.66	0.7	1.28	0.19	6.39	6.88	−7
	CM-300	2.03	5.30	0.27	0.71	0.13	3.94	4.32	−9
Geopolymeric matrix specimens	GM-200	3.89	2.39	0.98	1.17	0.29	7.56	7.34	+3
	GM-250	2.62	4.91	0.45	1.10	0.14	5.10	5.29	−4
	GM-300	3.82	2.13	0.95	1.01	0.33	7.43	7.89	−6

[1] Error = 100 × (predicted value − experimental value)/(experimental value).

To develop cohesive bond-slip models for the cementitious and geopolymeric carbon fabric-reinforced matrix composites, the average values of the parameters A and B were calculated and then plugged into Equations (4)–(7). The corresponding bond-slip models are depicted in Figure 10, whereas the corresponding key parameters are listed in Table 4. The slip at maximum shear stress, s_m, for the cementitious-matrix model was smaller than that of the geopolymeric-matrix model. The higher stiffness of the cementitious matrix model can be attributed to its higher Young's modulus relative to that of the geopolymeric matrix. Although the maximum shear stress, τ_m, of both models was equal, the fracture energy of the model for the geopolymeric-matrix joints was higher.

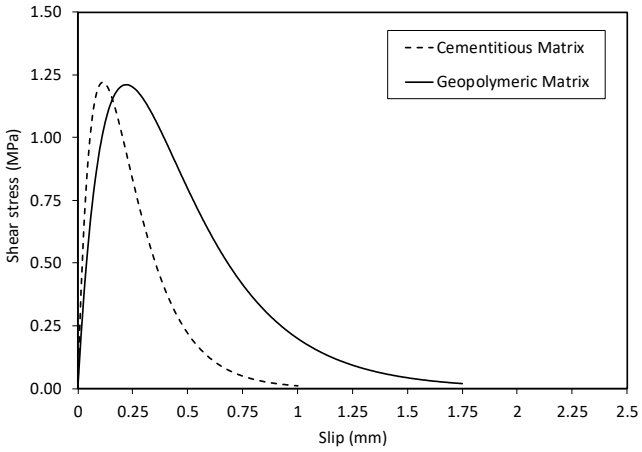

Figure 10. Bond-slip models.

Table 4. Parameters of the bond-slip models.

Matrix Type	A ($\times 10^{-3}$)	B (mm^{-1})	G_f (N/mm)	τ_m (MPa)	s_m (mm)
Cementitious matrix	2.48	6.11	0.40	1.22	0.11
Geopolymeric matrix	3.45	3.14	0.77	1.21	0.22

The maximum shear stress of the bond-slip model developed in the present study for carbon FRCM composites (1.22 MPa) is comparable to that published in the literature for PBO FRCM composites (1.32 MPa) [38]. Nevertheless, the slip at maximum shear stress (0.299 mm) and the fracture energy (0.997 N/mm) of the PBO FRCM bond-slip model [38] was higher than their respective values of 0.11 mm and 0.40 N/mm determined in the present study for carbon FRCM composites.

The bond-slip model developed in the present study for a nonmetallic composite-based system utilizing carbon fabrics and a geopolymeric matrix exhibited a lower maximum shear stress (1.21 MPa) and greater slip at maximum shear stress (0.22 mm) than those of the model developed by Bencardino et al. [24] for stainless steel-reinforced geopolymeric

matrix composites. The values of τ_m and s_m reported by Bencardino et al. [24] for stainless steel-reinforced geopolymeric matrix composites were 1.7 MPa and 0.12 mm, respectively. This implies that the bond between a nonmetallic carbon fabric and a geopolymeric matrix is inferior to that of stainless steel-reinforced geopolymeric matrix composites.

6. Conclusions

The bond behavior of nonmetallic carbon fabric reinforcement-matrix composites was examined in the present study. The potential use of a geopolymeric matrix rather than commercial mortars was investigated. The main conclusions of the work are summarized hereafter.

- The geopolymeric matrix employed in the current study can be used as a sustainable alternative to commercial cementitious mortars used in structural strengthening systems involving carbon fabric grids/textiles.
- The maximum loads of the geopolymeric-matrix specimens, except GM-250, were on average 71% higher than those of their cementitious-matrix specimens. The maximum load of GM-250 with a geopolymeric matrix was approximately 84% of that of CM-250 with a cementitious matrix.
- Three distinct modes of failure were observed in the present study; Mode I: slippage of the fabric without cracking of the matrix, Mode II: transverse/longitudinal cracks followed by slippage of the fabric and debonding at the fabric-matrix interface, and Mode III: rupture of the fabric.
- The effective bond length was approximately 170 mm for the cementitious-matrix specimens and 150 mm for the geopolymeric-matrix specimens.
- Specimen GM-300, with a geopolymer matrix, exhibited higher fabric strains near the loaded end and a steeper strain profile than those of specimen CM-300, with a cementitious matrix, which signified better bond at the fabric-matrix interface.
- New fabric-to-matrix interfacial bond-slip models were developed for specimens with cementitious and geopolymeric matrices. Although the maximum shear stress of both models was equal (1.2 MPa), the slip at maximum shear stress and the fracture energy of the geopolymeric-matrix model were higher. The handful of data points used to develop the bond-slip models should be expanded in future research to improve the soundness of the models.

Author Contributions: Conceptualization, T.E.-M. and H.E.-H.; data curation, F.A.O.; formal analysis, F.A.O. and T.E.-M.; funding acquisition, T.E.-M.; investigation, F.A.O.; methodology, F.A.O., T.E.-M. and H.E.-H.; project administration, T.E.-M.; resources, T.E.-M.; supervision, T.E.-M. and H.E.-H. All authors have read and agreed to the published version of the manuscript.

Funding: This research was funded by UAE University, grant number 31N372.

Institutional Review Board Statement: Not applicable.

Informed Consent Statement: Not applicable.

Data Availability Statement: The data presented in this study are available on request from the corresponding author. The data are not publicly available due to privacy issues.

Conflicts of Interest: The authors declare no conflict of interest.

References

1. ACI Committee 549. *Guide to Design and Construction of Externally Bonded Fabric-Reinforced and Steel-Reinforced Grout Systems for Repair and Strengthening of Concrete Structures*; American Concrete Institute: Farmington Hills, MI, USA, 2020.
2. Awani, O.; El-Maaddawy, T.; Ismail, N. Fabric-reinforced cementitious matrix: A promising strengthening technique for concrete structures. *Constr. Build. Mater.* **2017**, *132*, 94–111. [CrossRef]
3. Koutas, L.; Tetta, Z.; Bournas, D.; Triantafillou, T. Strengthening of concrete structures with textile reinforced mortars: State-of-the-art review. *J. Compos. Constr.* **2019**, *23*, 03118001. [CrossRef]
4. Donnini, J.; Corinaldesi, V.; Nanni, A. Mechanical properties of FRCM using carbon fabrics with different coating treatments. *Compos. Part B* **2016**, *88*, 220–228. [CrossRef]

5. Messori, M.; Nobili, A.; Signorini, C.; Sola, A. Mechanical performance of epoxy coated AR-glass fabric Textile Reinforced Mortar: Influence of coating thickness and formulation. *Compos. Part B* **2018**, *149*, 135–143. [CrossRef]
6. Signorini, C.; Nobili, A.; González, E.; Siligardi, C. Silica coating for interphase bond enhancement of carbon and AR-glass Textile Reinforced Mortar (TRM). *Compos. Part B* **2018**, *141*, 191–202. [CrossRef]
7. Pekmezci, B.; Çopuroglu, A. Mechanical properties of carbon-fabric-reinforced high-strength matrices. *Materials* **2020**, *13*, 3508. [CrossRef]
8. Wang, F.F.; Kyriakides, N.; Chrysostomou, C.; Eleftheriou, E.; Votsis, R.; Illampas, R. Experimental research on bond behaviour of fabric reinforced cementitious matrix composites for retrofitting masonry walls. *Int. J. Concr. Struct. Mater.* **2021**, *15*, 22. [CrossRef]
9. Hashemi, S.; Al-Mahaidi, R. Investigation of bond strength and flexural behaviour of FRP-strengthened reinforced concrete beams using cement-based adhesives. *Aust. J. Struct. Eng.* **2010**, *11*, 129–139. [CrossRef]
10. D'Antino, T.; Gonzalez, J.; Pellegrino, C.; Carloni, C.; Sneed, L. Experimental investigation of glass and carbon frcm composite materials applied onto concrete supports. *Appl. Mech. Mater.* **2016**, *847*, 60–67. [CrossRef]
11. Awani, O.; Refai, A.; El-Maaddawy, T. Bond characteristics of carbon fabric-reinforced cementitious matrix in double shear tests. *Constr. Build. Mater.* **2015**, *101*, 39–49. [CrossRef]
12. Barducci, S.; Alecci, V.; Stefano, M.; Misseri, G.; Rovero, L.; Stipo, G. Experimental and analytical investigations on bond behavior of basalt-FRCM systems. *J. Compos. Constr.* **2020**, *24*, 04019055. [CrossRef]
13. D'Ambrisi, A.; Feo, L.; Focacci, F. Bond-slip relations for PBO-FRCM materials externally bonded to concrete. *Compos. B Eng.* **2012**, *43*, 2938–2949. [CrossRef]
14. D'Ambrisi, A.; Feo, L.; Focacci, F. Experimental and analytical investigation on bond between Carbon-FRCM materials and masonry. *Compos. B Eng.* **2013**, *46*, 15–20. [CrossRef]
15. Sneed, L.; D'Antino, T.; Carloni, C. Investigation of bond behavior of polyparaphenylene benzobisoxazole fiber-reinforced cementitious matrix composite-concrete interface. *ACI Mater. J.* **2014**, *111*, 569–580.
16. Sneed, L.; D'Antino, T.; Carloni, C.; Pellegrino, C. A comparison of the bond behavior of PBO-FRCM composites determined by double-lap and single-lap shear tests. *Cem. Concr. Compos.* **2015**, *64*, 37–48. [CrossRef]
17. Ombres, L. Analysis of the bond between fabric reinforced cementitious mortar (FRCM) strengthening systems and concrete. *Compos. B Eng.* **2015**, *69*, 418–426. [CrossRef]
18. Carozzi, F.; Arboleda, D.; Poggi, C.; Nanni, A. Direct shear bond tests of fabric-reinforced cementitious matrix materials. *J. Compos. Constr.* **2020**, *24*, 04019061. [CrossRef]
19. D'Antino, T.; Sneed, L.; Carloni, C.; Pellegrino, C. Influence of the substrate characteristics on the bond behavior of PBO FRCM-concrete joints. *Constr. Build. Mater.* **2015**, *101*, 838–850. [CrossRef]
20. D'Antino, T.; Sneed, L.; Carloni, C.; Pellegrino, C. Effect of the inherent eccentricity in single-lap direct-shear tests of PBO FRCM-concrete joints. *Compos. Struct.* **2016**, *142*, 117–129. [CrossRef]
21. Ascione, L.; Felice, G.; Santis, S. A qualification method for externally bonded fibre reinforced cementitious matrix (FRCM) strengthening systems. *Compos. B Eng.* **2015**, *78*, 497–506. [CrossRef]
22. Vasconcelos, E.; Fernandes, S.; de Aguiar, J.B.; Pacheco-Torgal, F. Concrete retrofitting using metakaolin geopolymer mortars and CFRP. *Constr. Build. Mater.* **2011**, *25*, 3213–3221. [CrossRef]
23. Menna, C.; Asprone, D.; Ferone, C.; Colangelo, F.; Balsamo, A.; Prota, A.; Cioffi, R.; Manfredi, G. Use of geopolymers for composite external reinforcement of RC members. *Compos. B Eng.* **2013**, *45*, 1667–1676. [CrossRef]
24. Bencardino, F.; Condello, A.; Ashour, A. Single-lap shear bond tests on steel reinforced geopolymeric Matrix-concrete joints. *Compos. B Eng.* **2017**, *110*, 62–71. [CrossRef]
25. Kachouh, N.; El-Hassan, H.; El-Maaddawy, T. Effect of steel fibers on the performance of concrete made with recycled concrete aggregates and dune sand. *Constr. Build. Mater.* **2019**, *213*, 348–359. [CrossRef]
26. ASTM C192/C192M-19. *Standard Practice for Making and Curing Concrete Test Specimens in the Laboratory*; ASTM International: West Conshohocken, PA, USA, 2019.
27. BS EN 12390-3. *Testing Hardened Concrete—Compressive Strength of Test Specimens*; British Standards: London, UK, 2009.
28. ASTM C39/C39M-20. *Standard Test Method for Compressive Strength of Cylindrical Concrete Specimens*; ASTM International: West Conshohocken, PA, USA, 2020.
29. ASTM C496/C496M-17. *Standard Test Method for Splitting Tensile Strength of Cylindrical Concrete Specimens*; ASTM International: West Conshohocken, PA, USA, 2017.
30. ASTM-C618. *Standard Specification for Coal Fly Ash and Raw or Calcined Natural Pozzolan For Use in Concrete*; ASTM International: West Conshohocken, PA, USA, 2015.
31. Ismail, N.; El-Hassan, H. Development and characterization of fly ash/slag-blended geopolymer mortar and lightweight concrete. *J. Mater. Civ. Eng.* **2018**, *30*, 04018029. [CrossRef]
32. El-Hassan, H.; Elkhouly, S. Performance evaluation and microstructure characterization of steel fiber-reinforced alkali-activated slag concrete incorporating fly ash. *J. Mater. Civ. Eng.* **2019**, *31*, 04019223. [CrossRef]
33. El-Hassan, H.; Shehab, E.; Al-Sallamin, A. Effect of curing regime on the performance and microstructure characteristics of alkali-activated slag-fly ash blended concrete. *J. Sustain. Cem.-Based Mater.* **2021**, 1–29. [CrossRef]
34. El-Hassan, H.; Ismail, N. Effect of process parameters on the performance of fly ash/GGBS blended geopolymer composites. *J. Sustain. Cem.-Based Mater.* **2018**, *7*, 122–140. [CrossRef]

35. ASTM C109/C109M-20b. *Standard Test Method for Compressive Strength of Hydraulic Cement Mortars (Using 2-in. or [50 mm] Cube Specimens)*; ASTM International: West Conshohocken, PA, USA, 2020.
36. ASTM C469/C469M-14. *Standard Test Method for Static Modulus of Elasticity and Poisson's Ratio of Concrete in Compression*; ASTM International: West Conshohocken, PA, USA, 2014.
37. S&P ARMO Mesh. Available online: https://www.sp-reinforcement.eu/en-EU/products/reinforcement-mesh/sp-armo-meshr (accessed on 23 March 2021).
38. Zou, X.; D'Antino, T.; Sneed, L.; Carloni, C. Analytical bond-slip model for fiber-reinforced cementitious matrix-concrete joints based on strain measurements. *J. Mater. Civ. Eng.* **2019**, *31*, 04019247. [CrossRef]
39. Dai, J.; Ueda, T.; Sato, Y. Development of the nonlinear bond stress-slip model of fiber reinforced plastics sheet-concrete interfaces with a simple method. *J. Compos. Constr.* **2005**, *9*, 52–62. [CrossRef]